Research Article

Charged Ice Particle Beams with Selected Narrow Mass and Kinetic Energy Distributions

Anatolii Spesyvyi, Ján Žabka, Miroslav Polášek, Ales Charvat, Jürgen Schmidt, Frank Postberg, and Bernd Abel*

Read Online

ACCESS | Metrics & More | Article Recommendations | Supporting Information

ABSTRACT: Small ice particles play an important role in atmospheric and extraterrestrial chemistry. Circumplanetary ice particles that are encountered by space probes at hypervelocities play a critical role in the determination of surface and subsurface properties of their source bodies. Here we present an apparatus for the generation of low-intensity beams of single mass-selected charged ice particles under vacuum. They are produced via electrospray ionization of water at atmospheric pressure and undergo evaporative cooling when transferred to vacuum through an atmospheric vacuum interface. m/z selection is achieved through two subsequent quadrupole mass filters operated in the variable-frequency mode within a range of m/z values between 8×10^4 and 3×10^7. Velocity and charge of the selected particles are measured using a nondestructive single-pass image charge detector. From the known electrostatic acceleration potentials and settings of the quadrupoles the particle masses could be obtained and be accurately controlled. It has been shown that the droplets are frozen within the transit time of the apparatus such that ice particles are present after the quadrupole stages and finally detected. The demonstrated correspondence between particle mass and specific quadrupole potentials in this device allows preparation of beams of single particles with a repetition rate between 0.1 and 1 Hz with various diameter distributions from 50 to 1000 nm at 30−250 eV of kinetic energy per charge. This corresponds to velocities and particle masses quickly available between 600 m/s (80 nm) and 50 m/s (900 nm) and particle charge numbers (positive) between 10^3 and $10^4[e]$, depending upon size.
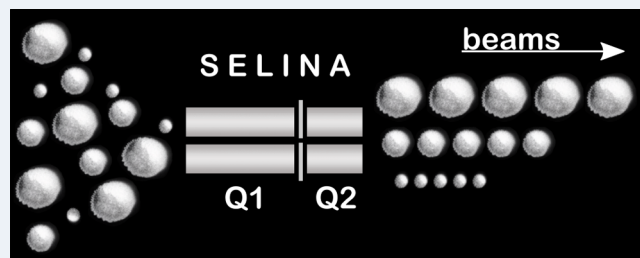
1. INTRODUCTION

Within the past few decades the interest in characterization of the features and composition of nanoparticles, aerosols, and dust has dramatically increased.[1] Powerful technologies are emerging for a precise synthesis, manipulation, and analysis of single particles, enabling a deeper understanding of impact phenomena related to atmospheric chemistry and space physics and chemistry. Theoretical and experimental studies of nanoparticle−surface collisions at low and high velocities have been reported.[2−4] Studies involving charged and neutral water particles in the nano- and micrometer size regime cover a wide range of research fields. This includes interface chemistry on the particle surface,[5] atmospheric chemistry,[6,7] lightning formation,[8] and water freezing and melting processes.[9,10]

Hypervelocity impact phenomena within the past 60 years have been motivated by the need to understand cosmic dust and micrometeoroid impacts onto instruments aboard space probes.[1,11] While larger particles can be accelerated with light-gas guns, smaller particles are more conveniently accelerated with electrostatic accelerators, because small particles can more easily achieve a sufficient charge to mass ratio.[2] In early works, smaller micrometer-sized charged particles have been accelerated with a Van de Graaff accelerator. A multistage laboratory-scale linear accelerator capable of accelerating particles to several thousand m/s became possible when powerful high-voltage switching electronics was available.[12] It should be emphasized here that all previous linear accelerators (except Continetti's recent work[2−4]) only worked for nonicy material.

The key to carrying out mass spectrometric measurements on individual charged nanoparticles is the use of image charge detection mass spectrometry techniques.[13−15] They determine the absolute charge on a particle from the magnitude of the image charge induced on a pickup electrode, when a charged particle passes through.[16] The image charge waveform also yields the particle time of flight (TOF) and velocity through the charge induction, providing the mass to charge ratio for fixed energy particles. This method has been used in accelerator experiments for many decades, and with the increasing interest in studies of massive biomolecules, cells, and nanoparticles, it
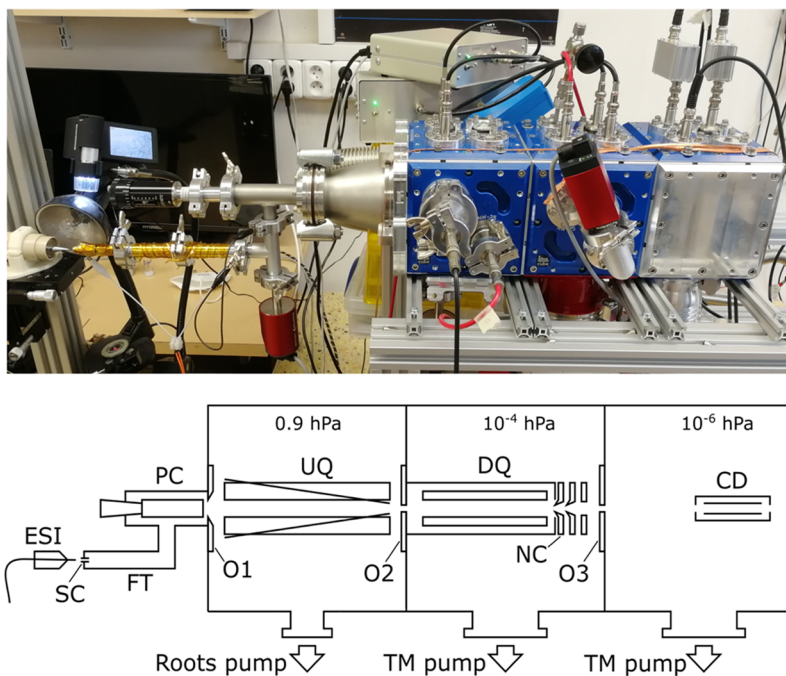
Figure 1. Photo of the SELINA apparatus and its schematic representation with indicated electrospray ionization source (ESI), sampling capillary (SC), flow tube (FT), plenum chamber (PC), 5 mm orifice (O1), upstream quadrupole with slanted wires (UQ), 1 mm orifice (O2), downstream quadrupole in enclosure (DQ), nose cone (NC), 2 mm orifice (O3), and charge detector (CD).

enabled more recent applications in mass spectrometry measurements, which were reviewed by Jarrold et al.[15] Continetti and co-workers recently highlighted ice particle acceleration and analysis in an aerosol impact spectrometer (AIS).[2−4]

Cosmic dust in the form of nanometer- to micrometer-sized ice grains originates from comets,[17] plumes from icy satellites of the giant planets,[18−21] or ejecta from hypervelocity impacts of micrometeoroids on the icy surfaces of atmosphereless bodies.[22−24] The plume of Enceladus ejects material from the subsurface ocean so that it may be sampled and analyzed from spacecraft on a fly-by or in orbit around the moon.[25] The Cosmic Dust Analyzer (CDA) instrument[26] on the Cassini spacecraft sampled Enceladus plume grains during flythroughs at 7−17 km/s relative velocity and returned fascinating findings about the grains' molecular composition,[27,28] including the presence of large organic macromolecules with masses of over 200 amu.[29] Terrestrial laboratory reproductions of the CDA mass spectra obtained from plume particles have demonstrated the sensitivity of the mass signatures to impact velocity.[30] There has been progress in producing laboratory analogues of the Enceladus plume grains in order to understand the measurements made by the Cassini probe.[27,29−32] Further quantitative laboratory analysis of high-speed impacts of ice particles with known composition, together with the resultant mass spectra, will serve as an invaluable calibration for future dust measurements with impact ionization dust mass spectrometers on future missions to study in situ material from the interior[25] or the surface of solar system icy satellites.[24] Testing how the high-speed impact of ice particles on a surface affects the resultant mass spectra would inform future missions to study plumes within our solar system, including the upcoming Europa Clipper mission to Europa. Moreover, any planetary surface of an icy body like Europa can be investigated by passing through the ejecta cloud produced by micrometeoroid impacts that form a constant exosphere surrounding any airless body.[33] The most prominent instrumental application of this method is the Surface Dust Analyzer (SUDA) instrument[34] aboard the Europa Clipper spacecraft that, during close fly-bys, will map the composition of encountered ejecta particles onto certain surface features of Europa.[24,35]

There have been few methods used to produce and study water particles and clusters under vacuum. Charged clusters/droplets are usually produced at atmospheric pressure by electrospray ionization (ESI), sonic spray, and aerosol generators and then are transferred to the vacuum for subsequent experiments.[13,36−39] Neutral particle beams are usually generated in the supersonic expansion through a conical nozzle,[40,41] or in Laval nozzles.[42] Also the particles/clusters could be ionized to low charge states by Na doping and photoinduced electron detachment.[43,44] Jarrold and co-workers[15] have recently demonstrated how to handle charged molecules and particles under vacuum and how to measure their charge and velocity for an ultimate and sensitive mass determination. They reported intriguing applications of charge detection mass spectrometry in molecular biology and biotechnology.[15] As interest in the characterization of nanoparticles, aerosols, and dust increases, the need for the development of new tools for the manipulation and analysis of single particles continues to grow. An interesting development in this direction was the aerosol impact spectrometer (AIS) recently developed by Continetti et al. that allows control of the energy and charge of aerodynamically focused and transferred charged particles to study surface−particle interaction and scattering.[2−4] An electrospray ion source coupled with a linear electrostatic trap was the basis of the ice particle accelerator, and a nine-stage linear accelerator was employed to control the final velocities of the nanoparticles.[2−4] Image charge detection (ICD) allowed for the determination of the absolute charge and mass of single nanoparticles.

In the present work, the development of a compact and versatile new ice-nanoparticle mass selector, accelerator, and spectrometer, different in concept from that of Miller et al., is described with a demonstration of its capabilities. Here, we present the first module of our apparatus "SELINA" (which stands for "selected ice nanoparticle accelerator"), which is able to generate and select charged ice particle beams within a range of 50−1000 nm diameter. In contrast to existing methods described above, our aim was to develop an instrument and technology to control properties of the beam and in turn of single particles such as mass, charge, and kinetic energy, while keeping the instrument reasonably compact and transportable—and compatible with an *n*-stage LINAC (linear accelerator) postacceleration unit for the investigation of hypervelocity particle beams (≥3−4 km/s) in the near future.[4]

2. EXPERIMENTAL SECTION

2.1. SELINA (Selected Ice Nanoparticle Accelerator). Figure 1 shows the SELINA apparatus and the schematics of its design, built for the preparation and mass selection of charged water ice nanoparticles. It is based on an IdealVac modular vacuum chamber system and consists of three 6 in. cubic aluminum frames and removable side plates with electric and pumping feedthroughs. Except for the mechanical pumps, all parts of the instrument are mounted on the mobile two 19 in. wide cart. Charged water droplets are generated by using a home-built electrospray ionization (ESI) source. Water with a minor admixture of formic acid (0.1% by volume) is sprayed from the 100 μm inner diameter (ID) silica capillary in front of the grounded 0.3 mm ID stainless steel 1/16 in. outer diameter (OD) 8 mm long sampling capillary (SC). A positive 4 kV voltage is applied to the metal needle of a syringe placed in a syringe pump operated at a 1 μL/min flow rate. The charged droplets from ESI are sucked together with air (at a 440 sccm flow rate) through the SC into a 20 cm long flow tube (FT) consisting of standard KF16 tubing. FT is followed by a T-cross, one end of which is used to mount the pressure gauge and another is connected to a plenum chamber (PC). The latter consists of a KF25/KF16 reduction T-cross with a KF25 end mounted on the instrument axis. A 13 mm OD aluminum rod fixed on a high-precision translation stage is attached coaxially to a PC. This assembly is then mounted on an ISO-K 63 flange with 5 mm orifice O1 onto the first vacuum chamber, which is evacuated with a multistage roots pump (Leybold, Ecodry65). The pressure (kept here at roughly 3 hPa) in the FT/PC and air flow rate are set by the position of the metal rod face relative to O1.

Particles and air entering SC gain supersonic velocities in the expansion due to a large pressure difference. Air molecules lose their momentum rapidly, and at some point the flow of air in FT becomes laminar. However, for water particles this process depends on their size and takes a longer time. Assuming laminar flow of air in the FT, entrained particles can be carried through the T-cross and enter the PC. Here again, following air streams around the metal rod in PC the particles reach O1 and pass through it to the first vacuum chamber. The PC design was introduced by the Reilly group[45] to effectively decrease velocities acquired by heavy ions during the supersonic expansion into vacuum.

The spacing between the metal rod and the orifice can be considered as an expansion slit, through which particles and air symmetrically expand to the center of the rod perpendicularly to O1. The resulting air jet carries charged particles into the

upstream quadrupole (UQ) housed in the first vacuum chamber with a typical pressure of 0.9 hPa. The UQ has 250 mm long hyperbolic rods and a field radius of 6 mm. Slanted 0.2 mm wire electrodes were added between the rods.[46,47] They were fixed on a large radius at the UQ entrance and on the quadrupole field radius at the exit. DC potential applied to the slanted wires helps to avoid trapping of charged particles in the long UQ at a relatively high pressure of 0.9 hPa by forming a weak drift field toward the UQ exit. The main purpose of the UQ is to thermalize particle energies gained by the expansion in O1 to the UQ electric potential U^{UQ}. A critical orifice O2 with 1 mm diameter separates the first UQ vacuum chamber and a second vacuum chamber, where the downstream quadrupole (DQ) enclosed in a metal tube is placed. The second DQ vacuum chamber is evacuated to 10^{-4} hPa by a turbomolecular pump (Pfeiffer, HiPace300), thus creating a constant mass flow of air between UQ and DQ chambers. O2 is the last orifice where charged particles gain some kinetic energy from the gas stream, dependent on their masses (i.e., cross sections). The DQ has 100 mm long cylindrical rods and a 2.6 mm field radius. The enclosure tube at the DQ exit ends with a 1 mm nose-cone orifice (NC), oriented inward into the quadrupole field. The NC is followed by a second 1 mm nose-cone orifice for ion extraction and focusing. After the filtering/mass selection in the DQ, charged particles pass through the grounded 2 mm orifice O3 into the third vacuum chamber pumped out with a turbomolecular pump (Pfeiffer, HiPace80) to 10^{-6} hPa. It contains a single-pass charge detector (CD) used to measure both the particle velocity and its charge. Operation of the quadrupoles and the charge detector will be described in the following sections.

2.2. Charge Detector. The charge detector (CD) is constructed of two 6.35 mm OD and 12.7 mm OD 50 mm long stainless steel tubes, which are mounted coaxially, and the ends of the larger tube are closed with caps having 2 mm diameter orifices on the CD axis. The outer tube is grounded, while the inner tube is connected to the charge-sensitive amplifier without a feedback resistor (Figure 2).[16]

The CD is fixed on a polypropylene holder together with the amplifier PCB directly inside the vacuum chamber. The amplified output signal is digitized by a 16-bit oscilloscope
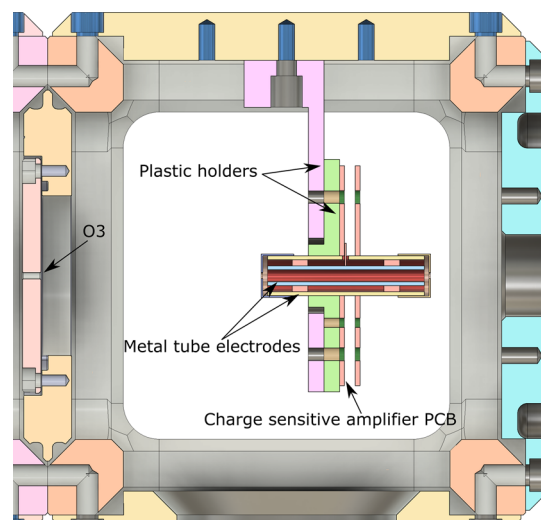

Figure 2. Schematic cross-section view of the image charge detector housed in the third vacuum chamber.

(PicoScope5000) and sent to the PC, where it is stored and processed by in-house-written software using the C# programming language. Charge detection mass spectrometry is an emerging analytical technique capable of mass determination of microparticles like viruses, proteins, exosomes, polymers, etc.[15]

The principle of operation of a single-pass charge detector has been described in detail previously.[48,49] Briefly, when a charged particle enters the inner tube, it induces an equal charge at the surface of the tube, which is kept until the particle leaves the tube. This induced charge is amplified and digitized, resulting in a voltage transient signal with two opposite peaks, corresponding to the charged particle entering and exiting the CD. The length of the tube divided by the time between the peaks yields the particle velocity. Figure 3 shows recorded signals for particles with different m/z, charge q ($=ze$, $e = 1.602 \times 10^{-19}$ C), and mass m in Da ($m = m$ (kg)$/u$, $u = 1.66 \times 10^{-27}$ kg).
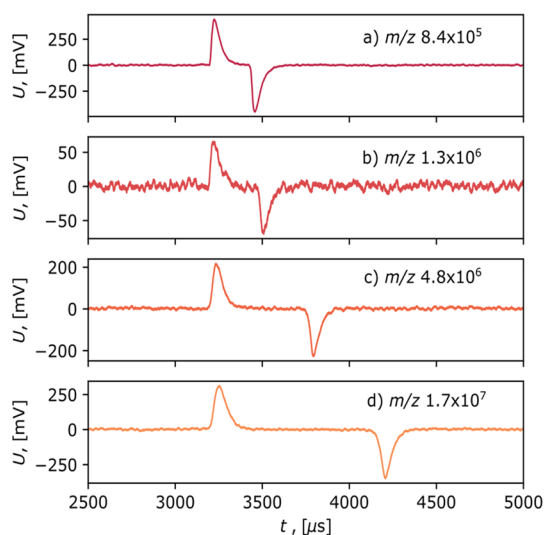

Figure 3. Typical signals of charged particles with 200 eV/z kinetic energy passing through the charge detector with the following properties: (a) $v = 214$ m/s, $q = 1.8 \times 10^4$ e, 8.4×10^5 m/z, $m = 1.5 \times 10^{10}$ Da; (b) $v = 172$ m/s, $q = 2.7 \times 10^3$ e, 1.3×10^6 m/z, $m = 3.5 \times 10^9$ Da; (c) $v = 90$ m/s, $q = 10^4$ e, 4.8×10^6 m/z, $m = 4.8 \times 10^{10}$ Da; (d) $v = 53$ m/s, $q = 1.7 \times 10^4$ e, 1.4×10^7 m/z, $m = 2.3 \times 10^{11}$ Da.

The charge of the particle can be derived from the amplitude of the first "entrance" peak and the known calibration constant. The calibration was done by injecting a known amount of charge (square pulse voltage through 0.8 pF capacity) directly on the inner tube of the detector. For our CD geometry and amplifier design the 1 mV response corresponds to 38 electron charges. However, when two charged particles possessing the same charge approach the detector with different velocities, the FWHM of the signal for the slower particle broadens and decreases in amplitude with respect to that of the faster particle. This dependence is corrected with the velocity-dependent coefficient (see the Supporting Information for more details). The signal-to-noise ratio of the amplifier allows us to measure particles with a charge down to 646 e (17 mV peak amplitude) or 950 e (25 mV amplitude) depending on the oscilloscope settings.

Once the charge q (and hence the charge number z) is known, m/z (and hence the mass itself) of the particle can be easily evaluated by taking into account the velocity v of the particle measured by the CD. Providing that the charged particle was

accelerated in an electrostatic field characterized by a potential difference U_a prior to the passage through the CD, the energy conservation (eq 1) allows one to get m/z easily (eq 2)

$$\frac{1}{2}muv^2 = U_a ze + \frac{1}{2}muv_0{}^2 \tag{1}$$

$$m/z = 2\frac{e}{u}U_a/(v^2 - v_0{}^2) \tag{2}$$

where v_0 is the particle velocity before the acceleration in the electrostatic field. Although the initial velocity v_0 is not known in our case, the voltage U_a is chosen so that the velocity achieved by the acceleration is much higher with respect to the initial velocity v_0. The value of m/z (i.e., m/z^{CD}) is then evaluated to a good approximation by neglecting v_0 in eq 2. In other words, non-negligible deviations of the particle kinetic energy from $U_a \cdot q$ will result in less reliable values of m/z^{CD}.

2.3. Quadrupoles Operated in the Variable-Frequency Mode. Both quadrupoles, UQ (high-pressure, RF-only transfer quadrupole) and DQ (low-pressure, RF/DC-resolving quadrupole), are operated in the frequency mode, i.e. the frequency of the sinusoidal AC voltage is changed to select the desired m/z, while the amplitude of the DC component and that of the AC component remain constant.[50,51] Such a mode of operation allows us to cover a wide range of m/z, a beneficial feature if high m/z values are to be detected. For this purpose, dedicated power supplies, QSwide1 and QSwide2, were developed (JanasCard, Czech Republic). QSwide1 is used for UQ and is capable of generating a constant amplitude of 100 V of the AC component in the 1−200 kHz frequency range with a variable DC component of ±35 V. QSwide2 is used for DQ, and it allows generating either the AC component with an amplitude of 100 V in the 0.5−200 kHz frequency range or 200 V with frequencies between 0.5 and 65 kHz. Here, the DC component can be varied by ±50 V. It is worth noting that 16-bit resolution of the DC component and a minimum frequency step of 0.03725 Hz can be achieved, allowing us to set the theoretical m/z in the DQ with a high precision. Both power supplies can float on the external DC potential up to ±1 kV. Considering the field radius of the quadrupoles, the m/z range accessible for UQ is from 1×10^3 to 4×10^7 and for DQ is from 5×10^3 to 1×10^9.

Because the quadrupole resolution is controlled by the ratio of the DC component to the AC amplitude,[52,53] in our case with the AC amplitude being constant it is the DC voltage that governs the resolution. The latter achieves its maximum for the ratio U_{DC}/U_{AC} of the DC and AC amplitudes equal to ~0.168, i.e., at the apex of the Mathieu stability diagram. In this work UQ was used for charged particle thermalization and guiding[54] after the expansion through O1 and was operated in RF-only mode at zero resolution. The DQ was used for the mass selection, and the DC voltage was set to 90% of that necessary to attain the theoretical maximum resolution.

As an example, for m/z 5×10^5 the following quadrupole settings were used: $f = 27773.54$ Hz, $U_{AC} = 100$ V, and $U_{DC} = 0$ V for UQ and $f = 9028.28$ Hz, $U_{AC} = 200$ V, and $U_{DC} = \pm 30.06$ V for DQ. Figure 4 illustrates the results obtained for several different nominal m/z settings, namely m/z 3, 4, 5, and 8×10^5. The assessed values for m/z, charge, velocity, and mass are shown in Figure 4a−d, respectively. Specifically, Figure 4c demonstrates the filtering capabilities of the resolving quadrupole DQ. The shape of the distributions, particularly the width, depends sensitively on both the quadrupole resolution (AC/DC
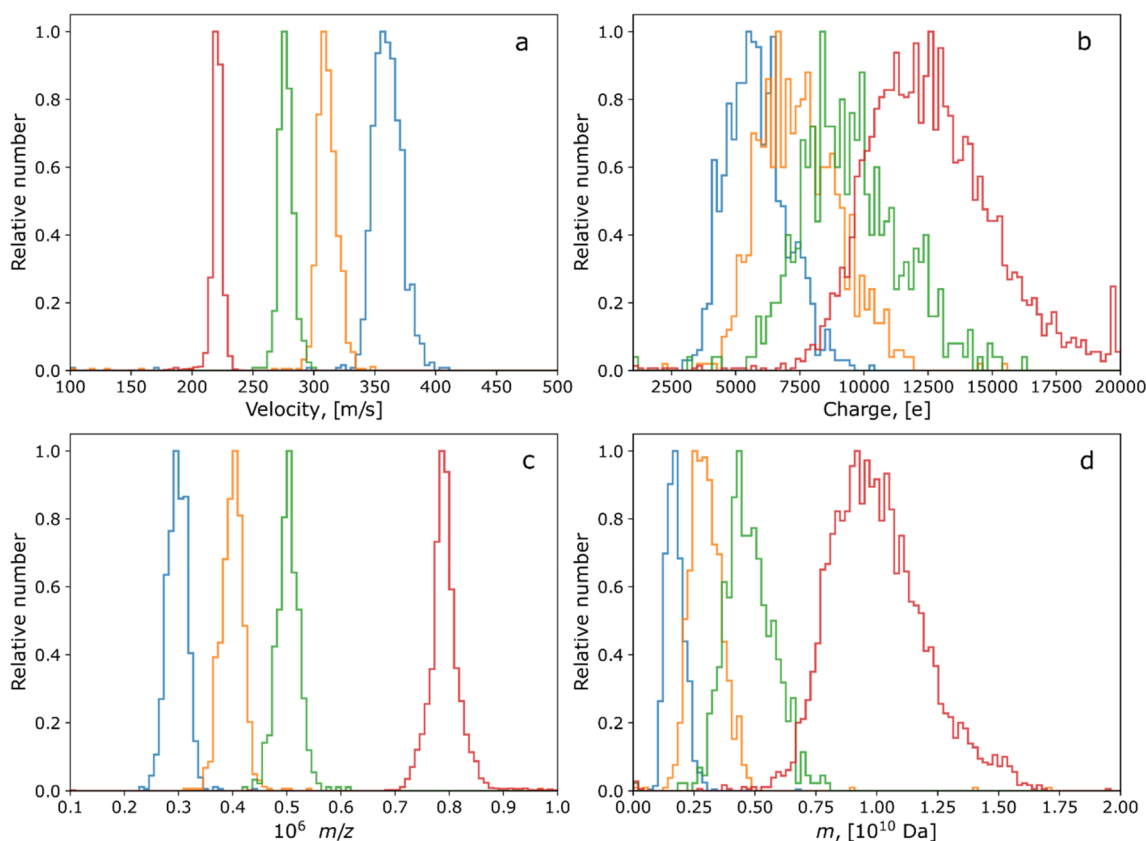
Figure 4. Normalized histogram distributions for particle velocities (a), charges (b), m/z (c), and masses (d) as measured with the charge detector when DQ is set to m/z^{DQ} 3×10^5 (blue), 4×10^5 (orange), 5×10^5 (green), and 8×10^5 (red) for U_a = 200 V.

ratio) and the spread in initial kinetic energy of charged particles as compared to the nominal acceleration voltage U_a.

This is usually accounted for in eq 2 by the initial particle velocity v_0 resulting from the drag force exerted by the air molecules on the charged particles during their pressure-driven expansion through O2 between UQ and DQ. The U_a value of 200 V used in eq 2 is defined by potentials U^{UQ} = 205 V, U^{O2} = 200 V, and U^{NC} = 200 V, as well as by the settings of the downstream quadrupole with U^{DQ} = 180, 175, 170, and 165 V for m/z 3×10^5, 4×10^5, 5×10^5, 8×10^5, respectively. The method of lowering the DC potential in DQ will be discussed later. From Figure 4c it is obvious that the mean m/z^{CD} assessed by CD reproduces very well the (nominal) values of m/z^{DQ} to which the resolving quadrupole was preset.

2.4. Polystyrene Bead Mass Measurement. Uniform polystyrene latex beads with nominal diameters of 100 and 600 nm in aqueous suspension with 10% of solid fraction (Sigma-Aldrich) were used to verify the accuracy of the mass detection. Modified ESI parameters (voltage +6 kV, flow rate 0.5 μL/min) were used, and measures to promote desolvation were undertaken, specifically the application of a resistive heating of the FT to 50 °C and the use of a bulb whose radiation heated the instrument entrance. The sample solutions were prepared by taking 20 μL of a 100 nm bead suspension dissolved in 2 mL of methanol or by taking 10 μL of a 600 nm bead suspension dissolved in a mixture of 1 mL of methanol and 2 mL of water.

3. RESULTS AND DISCUSSION

3.1. Mass Measurement Verification. The accuracy of the mass measurement by CD was tested using polystyrene latex beads with diameters of 100 and 600 nm, respectively.

Considering the mass density of 1050 kg/m³, their masses correspond to 3.3×10^8 and 7.2×10^{10} Da.

Charge detector measurements were done during the m/z scan of UQ adjusted to broad-band transmission and DQ with voltage settings corresponding to 0.9 of the maximum theoretical resolution in the range $1 \times 10^5 < m/z < 5 \times 10^5$ for 100 nm beads and in the range $1 \times 10^6 < m/z < 1 \times 10^7$ for 600 nm beads. The quadrupole potentials were adjusted to U^{UQ} = 60 V and U^{DQ} = 50 V for 100 nm beads and U^{UQ} = 260 V and U^{DQ} = 250 V for 600 nm beads. Only events where m/z^{CD} and m/z^{DQ} were within 10% deviation were used, which is particularly important for the 100 nm case, where the particle charge is close to the detection limit and noise distortions of the CD signal are noticeable. It can be seen in Figure 5 that there is a reasonable agreement between measured mass distributions and that calculated from the bead diameters: viz., 110 ± 10 and 610 ± 10 nm.

However, for 100 nm beads (Figure 5a) the mean of the measured mass distribution turns out to be shifted toward the lower boundary of the specified range. As mentioned earlier, particle charges in this case were close to the detection limit and the signals were hence affected strongly by the noise. Moreover, some of the maxima seen in the m/z distribution in Figure 5a may be due to residual solvent particles. For the 600 nm beads (Figure 5b), apart from the main peak with the expected mass, an additional broader peak centered at $\sim$3 $\times 10^{10}$ Da appeared. It corresponds to particles with a diameter of roughly 450 nm. The origin of such particles is not clear. Tentatively, it could arise from some contaminations of the sample or might be due to the prolonged ultrasonication necessary for the preparation of the diluted sample.
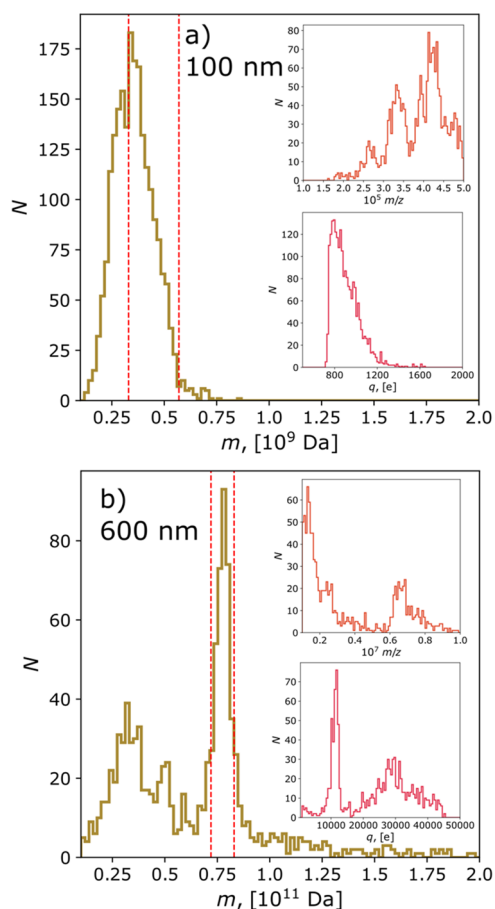
Figure 5. Mass distributions of polystyrene beads with nominal diameters 100 nm (a) and 600 nm (b). The insets show m/z and charge distributions assessed by CD. Red dashed lines indicate the mass range for the specified diameter range according to the specifications of the manufacturer.

3.2. Effect of the Downstream Quadrupole Potential U^{DQ} on the Mass Distribution.

As shown in Figure 4, only a relatively narrow m/z distribution of charged particles can be transmitted through the DQ, and thus the particle mass distribution turns out to be controlled to a large extent by the charge distribution. In the beginning we supposed that a selected m/z setting would result in charged particle distributions with a broad range of charges as well as masses. In the experiment, the DQ potential (higher with respect to O2 and UQ) would allow passing particles with enough kinetic energy per charge; hence, preferentially the particles should be the heavier ones. However, our experimental findings surprisingly showed that the opposite was true: i.e., filtering out of heavy particles with the higher charge occurred. On the other hand, when the DQ potential was lowered below UQ, O2, and NC particles with higher charges were detected. In fact, for the same m/z this means that higher masses have been preferentially transmitted toward CD. These effects are illustrated in Figure 6, where series of distributions were obtained by lowering (top row) and increasing (bottom row) the DQ potential in steps of 10 V.

One may argue that by lowering the DQ potential with regard to O2 and NC, a linear trap configuration with the residual gas from the first chamber arises. The relaxation of the initial particle kinetic energy gained in O2 can be clearly observed by inspecting the velocity distributions in Figure 6a. The smaller the kinetic energy, the closer the value m/z^{CD} detected to the m/z^{DQ} 5×10^6 preset in the resolving quadrupole (Figure 6b).

3.3. Mass and Kinetic Energy Selected Charged Particles.

To demonstrate the capability of the SELINA, we succeeded by means of adjustment of both quadrupoles and potentials in preparing nine particle beams with masses corresponding to particles with diameters between 50 and 1000 nm. Particle properties such as velocity v, m/z^{CD}, charge q, and mass m were obtained from the CD measurement, and their mean values are summarized in Table 1. Considering that the range of droplet sizes produced in ESI extends over a broad m/z
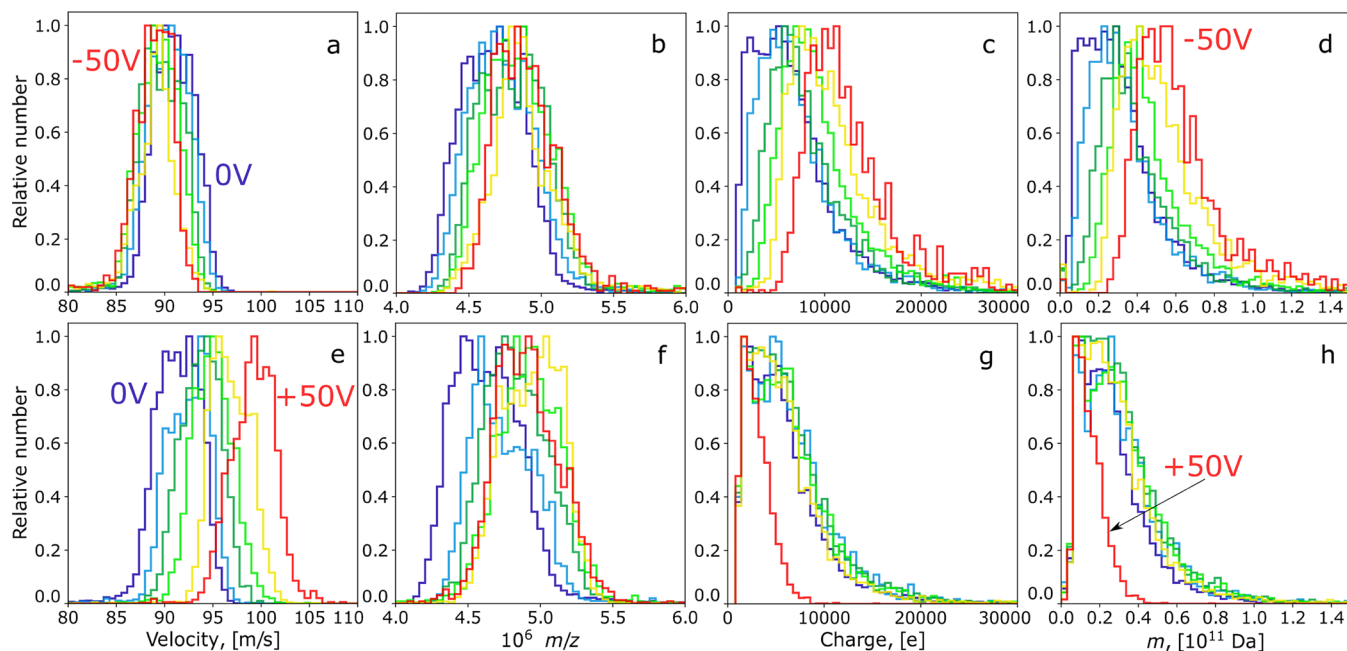

Figure 6. Velocity, m/z, charge, and mass histograms of the particles when DQ is set to m/z^{DQ} 5×10^6 at different DQ voltage potentials: from 200 to 150 V (top) and from 200 to 250 V (bottom) in 10 V steps. Potentials are designated in reference to 200 V.

Table 1. Settings Used to Prepare Nine Mass Distributions and Particle Properties: Upstream Quadrupole m/z^{UQ}, UQ Frequency f^{UQ}, UQ Potential U^{UQ}, Slanted Wire Potential U^{SW}, O2 Potential U^{O2}, Downstream Quadrupole m/z^{DQ}, DQ Frequency f^{DQ}, DQ AC Amplitude U_{AC}^{DQ}, DQ DC Component U_{DC}^{DQ}, Nose Cone Potential U_{NC}, Acceleration Voltage Used in CD Calculations U_a, Mean Value of Particle Velocity $\langle v \rangle$, m/z $\langle m/z^{CD} \rangle$, Charge $\langle q \rangle$, Mass $\langle m \rangle$, and Average Count Rate $\langle I \rangle$

	beam								
	1	2	3	4	5	6	7	8	9
m/z^{UQ}	8×10^4	1.5×10^5	2×10^5	3×10^5	5×10^5	8×10^5	1.5×10^6	5×10^6	3×10^7
f^{UQ}, Hz	21926.8	16013.1	13867.7	11322.9	8770.7	6933.9	5063.8	2773.5	1132.3
U^{UQ}, V	35	35	205	205	205	205	205	205	205
U^{SW}, V	20	20	195	195	195	195	195	195	195
U^{O2}, V	30	30	200	200	200	200	200	200	200
m/z^{DQ}	8×10^4	1.5×10^5	2×10^5	3×10^5	5×10^5	8×10^5	1.5×10^6	5×10^6	3×10^7
f^{DQ}, Hz	50555.4	36896.8	45192.4	36888.2	28564.8	22577.5	16485.5	9028.3	3686.3
U_{AC}^{DQ}, V	99.82	99.7	199.42	199.3	199.18	199.09	199.02	199.0	199.0
U_{DC}^{DQ}, V	±15.08	±15.06	±30.12	±30.11	±30.09	±30.07	±30.06	±30.06	±30.06
U^{DQ}, V	30	27	190	180	170	165	160	160	200
U^{NC}, V	29	30	200	200	200	200	200	200	250
U_a, V	30	30	200	200	200	200	200	200	250
$\langle v \rangle$, m/s	272	203	437	361	277	221	162	89	40
$\langle m/z^{CD} \rangle$	7.9×10^4	1.4×10^5	2.0×10^5	3.0×10^5	5.0×10^5	8.0×10^5	1.5×10^6	4.9×10^6	3.0×10^7
$\langle q \rangle$, e	9.2×10^2	1.9×10^3	3.2×10^3	5.8×10^3	9.5×10^3	1.3×10^4	1.5×10^4	1.3×10^4	7.3×10^3
$\langle m \rangle$, Da	7.3×10^7	2.7×10^8	6.5×10^8	1.7×10^9	4.8×10^9	1.0×10^{10}	2.2×10^{10}	6.5×10^{10}	2.2×10^{11}
$\langle I \rangle$, c/s	2.1	1.2	1.7	2.9	1.2	1.2	0.5	0.4	0.2

range, the most straightforward way to prepare charged particles with the required mass distribution is to scan a few values of quadrupole m/z settings. In order to select particles with the desired mass, the control software lets the quadrupoles scan over several m/z values and displayed the results in real time. As soon as measured mass values are in the desired range, the method of U^{DQ} lowering, which was described above, was applied to sample the high-mass side of the mass distribution. The mass distributions obtained in this way together with estimated particle diameters assuming spherical particles with the density of hexagonal ice (i.e., 917 kg/m³) are shown in Figure 7.[55] The assumption of frozen solid particles during detection by the CD will be justified in Section 3.8.

For most of the particles in Table 1 the setting U_a = 200 V was used. This value is suitable to accelerate particles in the m/z range from 2×10^5 to 2×10^7 with velocities that can be assessed by the CD. On the other hand, a lower potential of U_a = 30 V had to be applied for m/z between 8×10^4 and 1.5×10^5 to prevent the peaks detected by CD (see Figure 3) to overlap, which would otherwise be the case at U_a = 200 V.

As this effect might influence to some extent the charge (and m/z) measurement because of alteration of ion trajectories in front of and within the CD, we aim in the future to improve the design by implementing faster electronic circuitry to be able to detect particles with velocities beyond 500 m/s. Noteworthy as well, for the lightest particles (beams 1 and 2) the value of U_{AC}^{DQ} = 100 V instead of 200 V (beams 3−9) was used since the DQ frequency would have been out of range otherwise.

3.4. Estimation of the Charged Particle Residence Time in the FT and UQ. To understand what the aggregate state (solid or liquid) of the measured particles at the exit of the SELINA apparatus is (initially in the liquid state), we first estimated the residence time scales in the FT and UQ regions. For the former we assumed that particles after expansion at some point move together with the laminar air flow after the supersonic jet has dissipated. The velocity of gas v_g is calculated as[56]
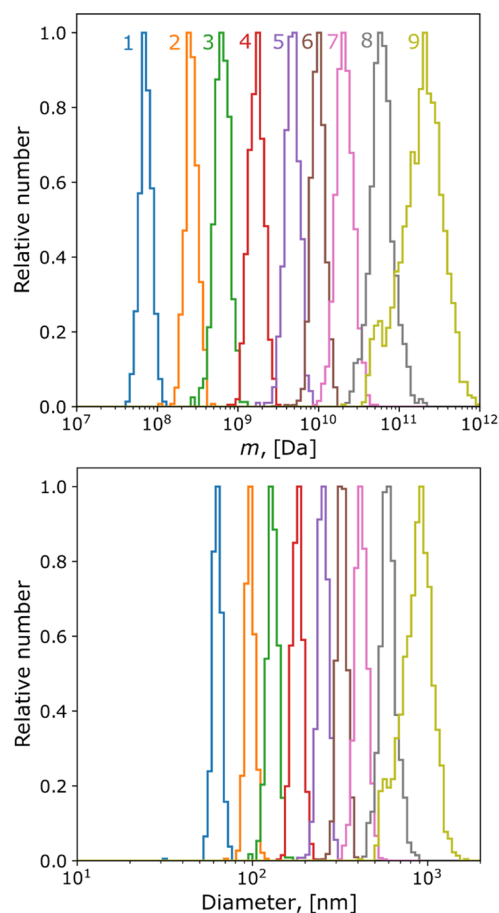

Figure 7. Selected mass (top) and corresponding diameter (bottom) distributions obtained with the settings listed in Table 1. The distributions are plotted as normalized histograms with a variable bin size for logarithmic representation.

Table 2. Calculated Mobilities K, Drift Velocities v_d, and Residence Times t_{50} Corresponding to the Drift Length Equal to 1/2 of the UQ Length

	beam								
	1	2	3	4	5	6	7	8	9
U^{UQ}, V	35	35	205	205	205	205	205	205	205
U^{SW}, V	20	20	195	195	195	195	195	195	195
E, V cm^{-1}	0.6	0.6	0.4	0.4	0.4	0.4	0.4	0.4	0.4
$\langle q \rangle$, e	9.2×10^2	1.9×10^3	3.2×10^3	5.8×10^3	9.5×10^3	1.3×10^4	1.5×10^4	1.3×10^4	7.3×10^3
$\langle m \rangle$, Da	7.3×10^7	2.7×10^8	6.5×10^8	1.7×10^9	4.8×10^9	1.0×10^{10}	2.2×10^{10}	6.5×10^{10}	2.2×10^{11}
D, nm	60	100	130	180	260	330	420	600	910
K, cm^2 V^{-1} s^{-1}	298	258	240	231	190	155	106	46	11
v_d, m/s	1.8	1.6	1.0	0.9	0.76	0.62	0.43	0.19	0.05
t_{50}, ms	70	80	130	140	170	200	290	670	2740

$$v_g = \frac{1}{A} \frac{\Phi}{p} \frac{T_g}{T_{20}} \tag{3}$$

where A = 0.785 cm^2 is the FT cross section, p = 3 hPa is the air pressure, Φ = 440 sccm is the air flow rate through the SC in the SELINA as measured with a flow meter, T_g is the air temperature, and T_{20} is 293 K usually used to calibrate flow meters. This calculation gives 12 m/s for air velocity in the FT. Particles with different masses lose their momentum after the expansion in SC and start moving with air flow in FT at different distances. However, only those charged particles that are carried by the air flow can pass the turn in T-cross on the way to the PC (see Figure 1). From the known length of 66 mm of this turn and the gas velocity from eq 3 we obtain 5 ms for the residence time particles need to make the turn. The overall dwell time in FT and PC at 3 hPa before entering the UQ chamber may accordingly be even longer. The motion of the charged particles exiting the plenum chamber through the O1 orifice is governed by the jet of air molecules formed in the expansion from 3 hPa in the PC to 0.9 hPa in the UQ chamber across O1. The kinetic energy the particles gain due to the drag force exerted by the accelerated gas molecules in the jet is obviously large enough to overcome the electrostatic potential barrier of the UQ (up to 200 eV per charge), suggesting that the air jet from the O1 dissipates inside the UQ. The stopping distance for the particles in the UQ depends on the particle size. For example, for a 200 μm diameter particle expanded from a 2 Torr aerodynamic lens to a 0.02 Torr chamber, the stopping distance in buffer gas was estimated to be about 40 cm.[57]

Considering the plenum chamber effect of the dumping air jet velocity and more than 1 order of magnitude higher pressure in the UQ chamber, it is reasonable to suggest that particles are stopped in the UQ or at least substantially slowed down in our setup. As a result, charged particle movement in the axial direction is governed by the drift field created by the imposition of the slanted wire potential U^{SW} on the UQ potential U^{UQ}. On the other hand, the radial motion of the particle is defined by the sinusoidal alternating electric field with 100 V amplitude and specific frequency for a particular m/z value. To estimate the residence time of the charged particle in the UQ, we can take a conservative approach and assume particle motion in the constant axial electrostatic drift field. The velocity v_d of the drifting particle can be derived from the known electric field E and charged particle mobility K as $v_d = KE$, where the mobility K can be calculated from the well-known formula[15,58]

$$K = \frac{3q}{16N} \sqrt{\frac{2\pi}{\mu k_B T}} \frac{1}{\Omega} \tag{4}$$

where q is the particle charge, N is the buffer gas density at 0.9 hPa, μ is the reduced mass, k_B is the Boltzmann constant, T is the buffer gas temperature, and Ω is the average momentum transfer cross section. The last quantity can be approximated by the cross section of the particle, $\pi(D/2)^2$, if it has a convex form and size above ~10^9 Da.[58] Then the residence time reads simply as $t = l/v_d$. Table 2 contains the calculated mobilities, velocities, and residence times for charged particles for l taken as half of the length of the upstream quadrupole.

3.5. Particle Charges. The particle charges measured as a function of mass m/z for the present setup are displayed in Figure 8 in a double-logarithmic plot. While the expected increase in charge with increasing m/z is observed, we find a significant drop for m/z starting in the range between 10^6 and 10^7 and being very significant above $m/z > 10^7$.

In comparison with the classical Rayleigh charge limit (maximum of charge Q_R of a droplet[59] as a function of radius a) estimated via[60]

$$Q_R = 8\pi \sqrt{\varepsilon_0 \gamma a^3} \tag{5}$$

where $\varepsilon_0 = 8.8 \times 10^{-12}$ F/m is the vacuum permittivity and $\gamma = 0.072$ N/m is the water surface tension.

We find that the results for m/z between 8×10^4 and 2×10^6 are close to (but above) the Rayleigh limit but deviate significantly toward lower values for $m/z \approx 10^7$. The dramatic decrease for $m/z > 1.5 \times 10^6$ may indicate a change in the charging mechanism or decharging. It may be possible and speculated that the particles undergo fragmentation from more massive particles losing charge on their way from ESI to DQ. Positive deviations from the Rayleigh limit may be explained by fragmentation of partly frozen icy particles producing highly charged secondary ice particles.[61] Since the charge of the parent particle is located mostly at the surface, the expansion of ice during further inward freezing results in an increase in pressure inside the ice shell, which may in turn produce highly charged fragments through ice layer splintering. A good review of these processes is given in ref 61.

3.6. Real-Time Mass Selection. As the selection of mass of the charged particles is based on the m/z and electric potential settings, it is possible to change the mass distribution of the particles in the current apparatus readily in real time. Figure 9 shows repetitive switching between m/z 2×10^5 (U^{DQ} = 195 V, U_a = 200 V) and m/z 1.5×10^6 (U^{DQ} = 160 V, U_a = 200 V).

Apparently, different masses with defined velocities and charges can be selected within tens of seconds by tuning the quadrupoles.
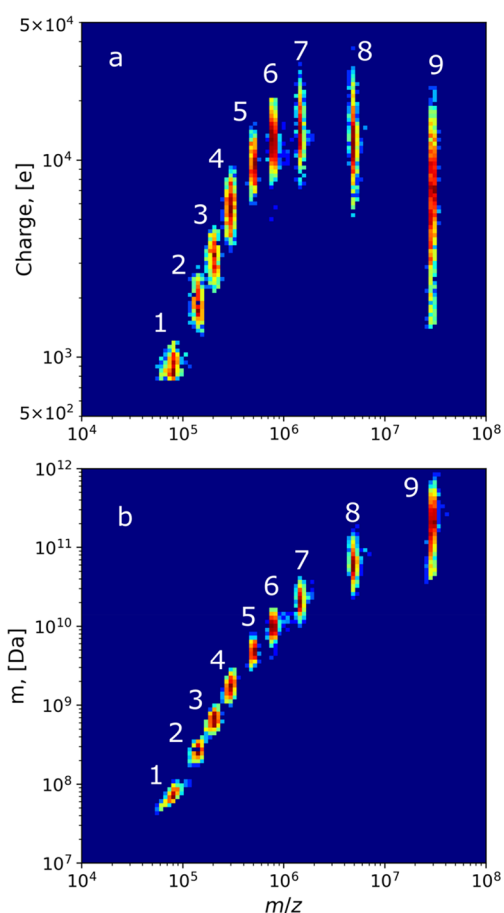
Figure 8. Superimposed m/z vs charge (a) and mass (b) 2D histograms of data measured by CD at the settings from Table 1. 2D histograms are built using variable logarithmic bins and a log-normal color map, where red is for the outcome with the highest number of appearances and dark blue stands for no outcome detected.
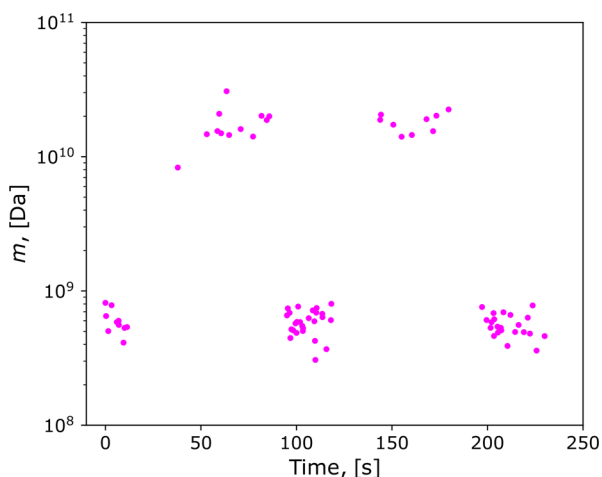

Figure 9. Particle masses assessed by CD while switching between two DQ settings for 4 min.

We also emphasize that the mass selection can be done between 50 nm and 1 μm with the present setup, enabling a smooth, rather "democratic" sampling of mass sizes (Figure 10), nevertheless with some differences in the count rate (see Table 1).

3.7. Effect of Kinetic Energy. In some applications it is useful to have an opportunity to vary the particle kinetic energy and thus its velocity and flight time. In SELINA this is possible to achieve by setting the UQ and DQ potentials. Assuming relatively high pressure in the UQ vacuum chamber, it should be lower than ∼250 V. This gives approximately a 30−250 eV range of accessible kinetic energy per charge.

Figure 11 demonstrates measured particle properties at UQ and DQ m/z 1.5×10^6 but at different electrostatic potentials, which define nominal kinetic energy per charge. The U^{DQ} value was set 40 V lower than the U^{NC} value in all three cases.

The good agreement between m/z distributions (Figure 11b) shows that the CD measurement works properly. The shape of the m/z distribution for U_a = 50 eV is slightly narrower and has wider tails with respect to the other settings. This may be due to an increased importance of the particle kinetic energy spread gained in the gas flow in O2 and in the quadrupole AC field (200 V AC amplitude) as compared to the kinetic energy due to the accelerating voltage.

3.8. Time Scales of Ice Grain Formation. Although the electrospray source initially forms liquid droplets that in turn shrink due to evaporation and eventually disintegrate further by Coulomb fission, all droplets rapidly freeze in the low-pressure regime and under vacuum in our setup. Depending on the transit time of the particles in the apparatus and the cooling as well as nucleation mechanism the particles are detected as ice grains in the image charge detector. In any case the liquid droplets pass a rapid cooling phase, a nucleation phase, and a sublimation phase. To obtain reliable estimates for the above time scales for particles with a defined size, phase, and temperature, and for a comparison with the transit times of the particles in our apparatus, we examine the numbers for a characteristic particle dimension: i.e., 1 μm in comparison with literature data.

To examine this, simple models for the dominant processes leading eventually to frozen microparticles were employed. The chronological sequence of these processes is as follows: the cooling by diffusion-controlled and free-molecular evaporation at high and low pressures, respectively, homogeneous nucleation of the meanwhile deeply supercooled droplet accompanied by an initial (∼isothermal) growth of ice germs, ice growth during recalescence (fast adiabatic phase with sharp temperature increase), the freezing of the rest of the specimen, and finally cooling of the ice particle through sublimation.

Entering the flow tube, the charged particles are surrounded by gas (air) at room temperature and a pressure of 3 hPa. The diffusion-controlled evaporation during the initial phase (i.e., at about atmospheric pressure) of the droplets has been estimated to be fast but relatively small in magnitude (see the Supporting Information) as opposed to the ballistic evaporative cooling occurring at low enough pressures, particularly under vacuum.

For the mean free path (MFP) being inversely proportional to the pressure, the value of the Knudsen number, Kn, defined as a ratio of the free mean path and droplet radius, attains a value of 10 for a 1 μm diameter droplet at a pressure (in air or water vapor) of about 10hPa, a value where free-molecular-flow conditions prevail. In such a regime the mass transfer is described by the Hertz−Knudsen−Langmuir (HKL) equation. Assuming for simplicity no vapor far from the droplet (i.e., $\rho_{V,\infty}$ → 0), the time evolution of the droplet mass (kg s^{-1}) and the droplet radius assume the following forms[62,63]
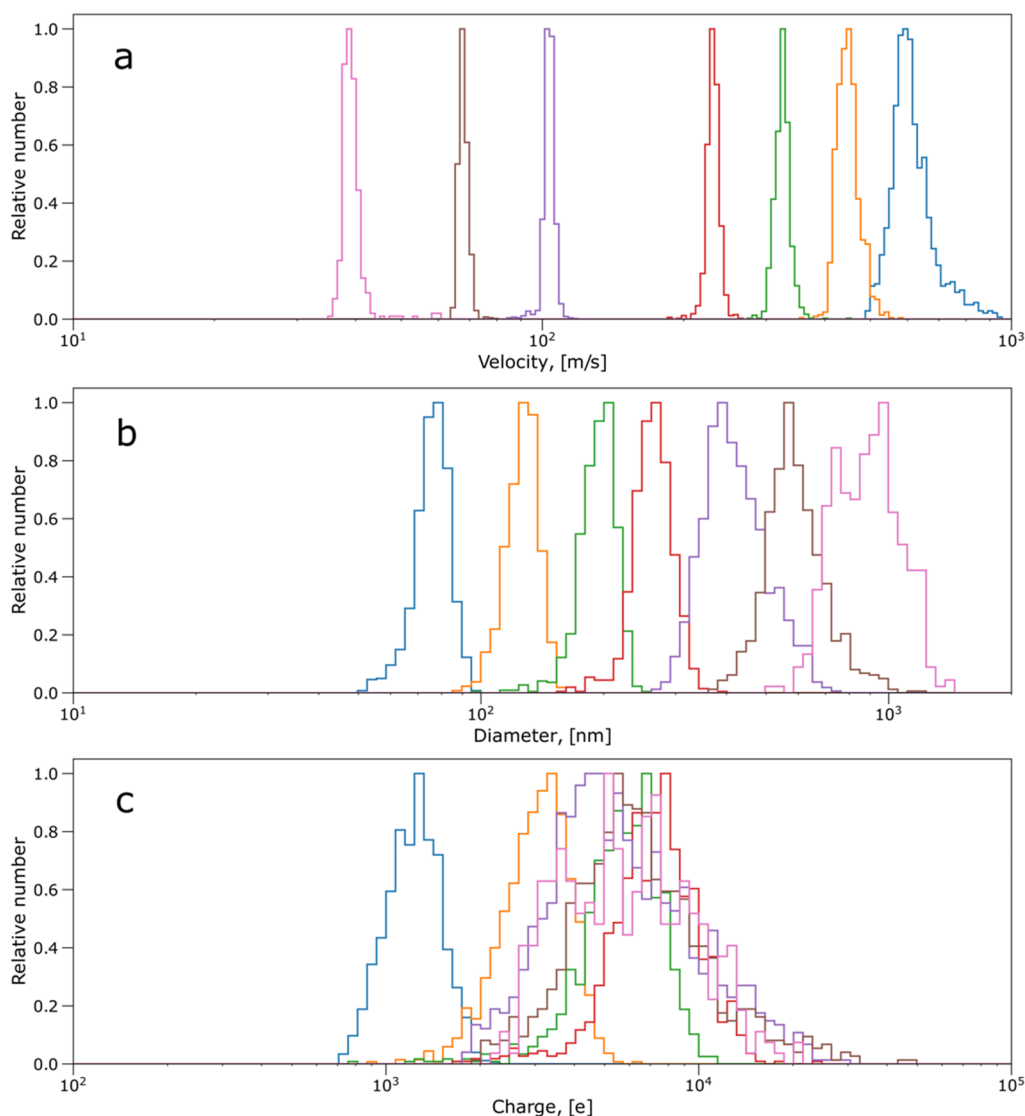
Figure 10. Ice grains sampled between 50 and 800 nm with kinetic energies and particle masses being quickly available between 600 m/s (80 nm) and 50 m/s (900 nm) and particle charge numbers between 10^3 and 10^4 [e] depending upon size.

$$\dot{m}_{HKL} \equiv 4\pi a^2 \cdot j_{m,HKL} = 4\pi a^2 \cdot \alpha \cdot \frac{1}{4} v(T_a) \rho_{V,a}(T_a)$$

$$\dot{a} = \frac{1}{4} \alpha v(T_a) \rho_L^{-1} \rho_{V,a}(T_a) \tag{6}$$

where α is the evaporation coefficient, v is the average thermal velocity of the vapor molecules, and ρ_V and ρ_L are the mass densities of the vapor and liquid, respectively.

By neglecting the radiative energy transfer, the only source for the latent heat of evaporation is the thermal energy of the droplet, provided the surroundings are such that other processes like convection and/or conduction are negligible. On evaporating, a small droplet cools down inevitably, and this occurs at an extraordinary high rate. During this process the droplet temperature T_a and hence the vapor density at the droplet surface, $\rho_{V,a}$ both vary significantly as the dwell time of the droplet in the low-pressure environment advances.

It might be instructive to realize that for an aqueous microdroplet a significant temperature drop corresponds to a rather small mass loss. Let Δm be the mass loss due to evaporation and Δa the corresponding change of the droplet

radius. The temperature change for a liquid droplet of initial mass m (and radius a) is then given by

$$\Delta T = -\frac{\Delta H}{c_p} \left(1 - \frac{m}{\Delta m}\right)^{-1} = -\frac{\Delta H}{c_p} \left(1 - \frac{1}{3} \frac{a}{\Delta a}\right)^{-1} \tag{7}$$

where c_p is the specific heat capacity of the liquid (J kg^{-1} K^{-1}) and ΔH is the latent heat of evaporation (J kg^{-1}). For water at room temperature, the ratio $\Delta H/c_p \simeq 2.2 \times 10^6/4.2 \times 10^3 \simeq 500$. If $\Delta m/m = 0.1$ (i.e., $\Delta a/a \simeq 0.03$), $\Delta T \simeq -50$ K. Note that for temperatures in the range 240 K $< T <$ 300 K the ratio of the latent and specific heats stays almost unchanged.

Based on the preceding equation, the temperature evolution can be iteratively evaluated by assuming the droplet mass (and hence the droplet radius) to a first approximation to be constant (i.e., $\Delta m \ll m$). Using eq 7 for $\Delta m/\Delta t$ we get

$$\Delta T_{a,HKL} \cong -a^{-1} \left[-\alpha \frac{3H}{c_p \rho_L} p_{V,a}(T) \left(\frac{M}{2\pi RT} \right)^{1/2} \right] \Delta t \tag{8}$$

The vapor pressure $p_{V,a}$ can be represented either by a Clausius−Clapeyron (CC) formula or by using parametrized
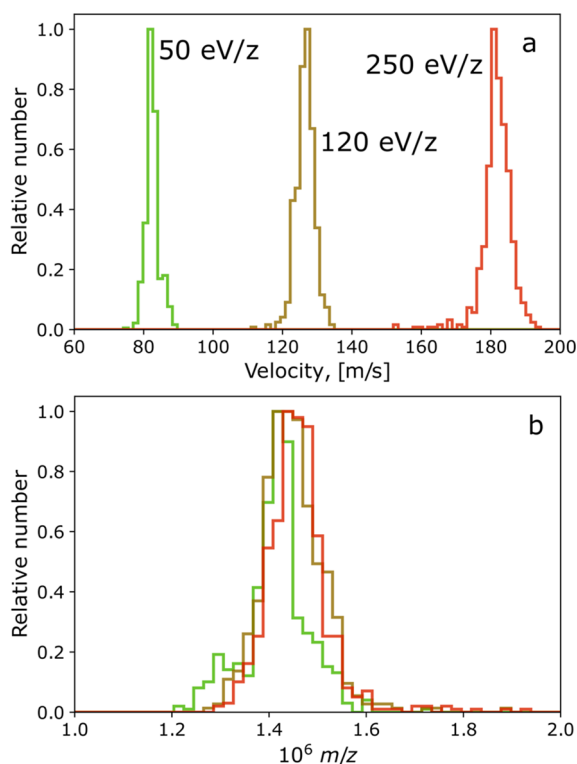
Figure 11. Histogram plots of the velocity (a) and m/z (b) distributions for three acceleration voltages U_a of 50 V (green), 120 V (brown), and 250 V (red).

expressions for the vapor pressure (see the Supporting Information).

In Figure 12 some of the calculated temperature transients are presented. Obviously, there are only minor differences between
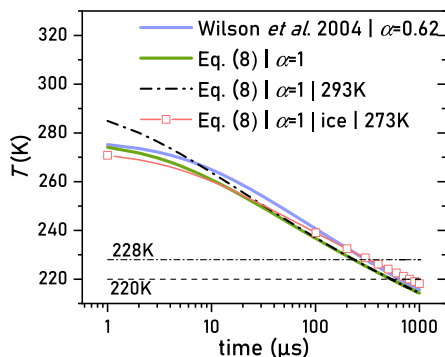

Figure 12. Temperature vs time for evaporative cooling in a ballistic regime. Comparison of evaporative cooling models for a 1 μm in diameter water (ice) droplet. At an initial temperature 277 K: blue line according to ref 64 using $\alpha = 0.62$, green line according to eq 8 taking $\alpha = 1$, and dashed-dotted line according to eq 8 for an initial temperature 293 K. The red curve represents the cooling of 1 μm diameter ice particles. The vapor pressures of liquid and ice were taken from ref 68.

predictions based on Wilson et al.[64] and ours based on eq 8. Depending on the model and parameter used and with an evaporation coefficient of 0.62, a value favored in ref 65, a temperature of 220 K will be reached for a 1 μm diameter droplet between 0.65 and 0.85 ms. This time will be even shorter if a larger evaporation coefficient has been used (e.g., 0.55 ms using $\alpha = 1$). In any case, this time appears in reasonable

agreement with the value retrieved from the investigations by Zilch et al.,[13] who found for a 0.47 μm radius droplet that it attained a temperature of 220 K after about 0.6 ms. The starting temperature has only a minor impact on the transient behavior of the temperature, as shown in Figure 12.

From the simulations it is obvious that the temperature for droplets with a diameter of about 1 μm can reach temperatures below 240 K and even cross the homogeneous nucleation temperature ($\sim$235 K) within a few hundreds of microseconds, resulting in deeply supercooled metastable microdroplets. Therefore, we anticipate that the bottleneck for freezing may be set by the homogeneous nucleation of water droplets in the supercooled temperature range. As discussed in more details in the Supporting Information, the time needed for the homogeneous nucleation of supercooled water has been experimentally determined for different supercooling, ΔT (=273.15 $- T$). Although not unanimously acknowledged (see the Supporting Information), we have applied volume nucleation rates according to a publication by Espinosa et al., who provided a smooth interpolation between different experimental data sets.[66,67] The corresponding nucleation time can be written as $t_N = [J_v V]^{-1}$ with J_v being the volume nucleation rate (m^{-3} s^{-1}) and V the droplet volume.

On the other hand, once a nucleus is created, the growth rate of the ice phase controls the kinetics of the freezing process. The former has been recently investigated by Xu et al.[69] using laser-induced heating of supercooled solid amorphous water, and following the subsequent crystallization of submicrometer thin samples the growth velocity could be assessed in a wide temperature range (11 K < ΔT < 147 K). Using both the nucleation and growth rates (for their numerical values see the Supporting Information), the time- and temperature-dependent fraction of the sample that turns *isothermally* into the ice can be evaluated using the Kolmogorov–Johnson–Mehl–Avrami (KJMA) relation:[66,67]

$$f_{KJMA} = 1 - \exp\left[\frac{\pi}{3} J_v G_{ice}^3 t^4\right] \tag{10}$$

Here, G_{ice} represents the growth rate of the ice nucleus (m s^{-1}) and t is the time. As G_{ice} and J_v are functions of the temperature, the frozen fraction can be evaluated at given supercooling as a function of the time (see the Supporting Information for details).

In fact, at significant levels of supercooling isothermal conditions can be maintained only during some (short) time, as the rapid growth of the crystalline phase (presumably on a microsecond time scale) results in a quasi-adiabatic increase of the temperature due to the release of the latent heat of crystallization. This is called the recalescence.[61]

After seeding by homogeneous nucleation and initial isothermal growth of the ice germs (following KJMA), the ice keeps growing during recalescence as well. At the end of the recalescence, the temperature of the droplet is supposed to be near the normal melting temperature: i.e., $\Delta T \lesssim 0$. The mass fraction f_{recal} of the ice phase built up during recalescence can be roughly estimated for a given supercooling by the corresponding Stefan number, i.e., $c_p \Delta T/L_f$[61] with c_p and L_f being the specific heat and the latent hat of fusion (crystallization), respectively. Both are temperature dependent. Using a temperature-averaged growth velocity, the time scale for the recalescence can be appraised as $t_{recal} \approx a/\overline{G}_{ice}$.[61]

The last step concerning freezing is the crystallization of the entire droplet. During the recalescence stage the latent heat of

crystallization has been absorbed at the expense of the droplet's temperature and has left the droplet in a two-phase state at about 273 K. To turn the rest $(1 - f_{\text{recal}})$ of the droplet mass into ice, the additional heat of crystallization must be drawn away by the combined effect of evaporative cooling due to the remaining liquid as well as that of the existing ice (sublimation). We have seen (Figure 12) that cooling rates in the ballistic regime for both the supercooled liquid and ice are comparable because of the close resemblance of the vapor pressure of the supercooled liquid and ice.[68] The amount of maximum supercooling attained in our experiments, and hence the time at which the homogeneous nucleation becomes significant and the freezing process begins, can be estimated by comparing the reciprocal of the droplet cooling rate, $(dT_a/dt)^{-1}$, with the nucleation time t_N at a given temperature/supercooling. The former represents a time span the droplet spends keeping its temperature within 1 K, and it has been evaluated straightforwardly with the help of eq 8.

Both quantities are shown in Figure 13 for a 1 μm diameter droplet. The two curves intersect at a temperature of about 228
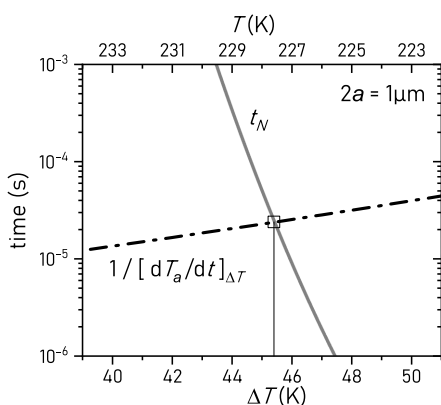

Figure 13. Time scales for a 1 μm diameter droplet: nucleation time (solid line), and the time spent at a temperature $T \pm 0.5$ K (dash-dotted line) given as the reciprocal of the (temperature-dependent) cooling rate. At $\Delta T \leq 45.4$ K, the nucleation becomes operative.

K. At that temperature (and below) the nucleation will be always (much) faster in comparison to the temporal evolution of the droplet temperature. At this point the freezing begins. Recalling Figure 12, a time of about 0.25 ms is needed to achieve a temperature of 228 K for a droplet of this size. For the Stefan number, at $\Delta T = 45.4$ K we get $f_{\text{recal}} \simeq 0.5$ for the values of specific and latent heat taken at the normal melting temperature. This may be a lower estimate, as the specific heat of the SCW increases as a function of supercooling[70] and the latent heat of crystallization on the other hand decreases upon increasing supercooling.

A rather conservative estimate for $\overline{G}_{\text{ice}}$ in the temperature range $0 < \Delta T < 50$ K is 0.01 ms^{-1} (see the Supporting Information). The recalescence time for $a = 0.5$ μm turns out to be 50 μs. Following recalescence, near the normal melting point the growth rate amounts to about 10^{-3} ms^{-1},[71] and if the *whole* droplet had to freeze under such conditions, it would take 0.5 ms, provided the latent heat of fusion can be efficiently channeled out of the droplet. Again, this is a rather cautious estimate, since a considerable part of the droplet has already been frozen at the end of the recalescence. Assuming $f_{\text{recal}} \simeq 0.5$, the time to complete the solidification will be 0.25 ms.

Considering the sum of the times of the different freezing stages estimated above, the complete freezing of a droplet with 1

μm diameter is finished within 0.6 $\pm$ 0.15 ms. Jarrold and colleagues used a different approach based on kinetics of homogeneous nucleation applied to large water clusters developed by Huang and Bartell.[40] According to their calculations provided in the paper by Zilch et al.,[13] a droplet with a radius of 0.47 μm entirely freezes within 0.52 ms. As far as particles of other sizes are concerned, smaller particles will freeze on a shorter time scale (e.g., about 100 μs for a 100 nm diameter particle), whereas larger particles need more time to freeze (e.g., roughly 5 ms for a 10 μm diameter particle) (see the Supporting Information for details). Therefore, we conclude here that as the time scale found for freezing is well below the transit times of the particles through the apparatus (see section 3.7), we are very confident about the fact that the particles detected by the CD are solid.

3.9. Accessible Particle Size Distribution of the Instrument. The distribution of droplets and finally ice particles is governed by the initial ESI source, the initial atmospheric pressure interface capillary, and the droplet charge from the ESI process and a sonic spray charging process within the capillary leading to size- and charge-dependent Coulomb explosions, which in turn result in a size distribution between 50 and 1000 nm in our present setup. It is interesting to note that the particle size can be selected easily within the size range of 50−1000 nm (diameter) with the instrument parameters (no strong bias against a certain size). Beyond Coulomb fission the primary and secondary droplets undergo rapid evaporative cooling, which in turn influence the size and temperature of the droplets and finally their aggregate state.

In experiments by Jarrold and co-workers,[72] pure water was electrosprayed and droplets were examined only in the vacuum stage of the instrument. Depending on the atmospheric pressure interface (i.e., orifice or capillary), droplet diameters in the range 0.5−5 μm were assessed. Applying the scaling laws,[15] values retrieved for the initial droplet diameter span the range 10−30 μm. In our case, an aqueous solution of formic acid (0.1 wt %) has an electric conductivity of 0.5 mS/cm.[73] At a flow rate of 1 μL/min the results of different scaling laws appear to be consistent and give a droplet diameter of about 0.6 μm. Of course, the above estimate does not take explicitly into account the influence of the voltage applied to the electrospray needle (capillary). Nevertheless, for low liquid flow rates, the influence of the applied voltage on the droplet diameter was found to be rather weak.[74,75]

4. SUMMARY AND CONCLUSIONS

We have presented the SELINA apparatus concept, which is able to produce a beam of well-characterized individual charged ice particles at a repetition rate of 0.1−1 Hz within a diameter range of 50−1000 nm at present. Very efficient positive charging of particles was observed, which resulted in particle charges between 10^3 and $10^4[e]$, depending upon the mass. The specific electrostatic potentials of the quadrupoles UQ and DQ, with pressures of 0.9 and 10^{-4} hPa, separated by the 1 mm orifice, allowed us to select particles with high charge and m/z. We want to point out that the important instrumental innovation here was to use quadrupoles in the variable-frequency mode to select charged particles in the 8×10^4 to 3×10^7 m/z range and to provide fast particles between 600 m/s (80 nm) and 50 m/s (900 nm) at high repetition rates with fast parameter control. This capability was verified by independent m/z measurements with an image charge detector. Although the full characterization of this mode of quadrupole operation (resolving power,

transmission) requires additional experiments, its potential is already obvious. With the present setup a relatively unbiased and fast *mass/size* selection is possible between 50 nm and 1 μm, enabling a smooth rather democratic sampling of mass sizes. The mass range of particles beyond 1 μm will be explored in the future. The time scales estimated for freezing are well below the transit times of the particles through the apparatus, which strongly suggests that the detected particles are in the ice phase. In comparison to existing concepts, we note that the current setup is a very compact and modular apparatus.

In future experiments the selected particles will be postaccelerated to study hypervelocity impacts. For this an *n*-stage LINAC is currently set up in our laboratory.[4] If necessary, the particles may be neutralized[76−78] or accelerated in front of a target through target biasing for the test of space mission relevant mass detectors.

■ ASSOCIATED CONTENT

ⓢ Supporting Information

The Supporting Information is available free of charge at https://pubs.acs.org/doi/10.1021/jasms.2c00357.

> Charge detector calibration, EHD atomization and general remarks, ESI droplet size with scaling laws vs experiments, droplet charge and its limits, and field-induced ion evaporation, and evaporative cooling and freezing of microdroplets (PDF)

■ AUTHOR INFORMATION

Corresponding Author

Bernd Abel − *Institute of Chemical Technology and Wilhelm-Ostwald-Institute of Physical and Theoretical Chemistry, D-04103 Leipzig, Germany; Leibniz Institute of Surface Engineering, D-04318 Leipzig, Germany;* ⓞ orcid.org/0000-0001-6032-1680; Email: bernd.abel@uni-leipzig.de

Authors

Anatolii Spesyvyi − *J. Heyrovský Institute of Physical Chemistry of the Czech Academy of Sciences, 18223 Prague 8, Czech Republic;* ⓞ orcid.org/0000-0003-0220-0519

Ján Zabka − *J. Heyrovský Institute of Physical Chemistry of the Czech Academy of Sciences, 18223 Prague 8, Czech Republic*

Miroslav Polášek − *J. Heyrovský Institute of Physical Chemistry of the Czech Academy of Sciences, 18223 Prague 8, Czech Republic*

Ales Charvat − *Institute of Chemical Technology and Wilhelm-Ostwald-Institute of Physical and Theoretical Chemistry, D-04103 Leipzig, Germany; Leibniz Institute of Surface Engineering, D-04318 Leipzig, Germany*

Jürgen Schmidt − *Institute of Geological Sciences, Freie Universität Berlin, D-12249 Berlin, Germany*

Frank Postberg − *Institute of Geological Sciences, Freie Universität Berlin, D-12249 Berlin, Germany*

Complete contact information is available at:
https://pubs.acs.org/10.1021/jasms.2c00357

Notes

The authors declare no competing financial interest.

■ ACKNOWLEDGMENTS

■ REFERENCES

(1) Grun, E.; Kruger, H.; Srama, R. The Dawn of Dust Astronomy. *Space Sci. Rev.* **2019**, *215* (7), 46.

(2) Adamson, B. D.; Miller, M. E. C.; Continetti, R. E. The aerosol impact spectrometer: a versatile platform for studying the velocity dependence of nanoparticle-surface impact phenomena. *Epj Technol. Instrum.* **2017**, *4*, 2.

(3) Belousov, A.; Miller, M.; Continetti, R.; Madzunkov, S.; Simcic, J.; Nikolic, D.; Maiwald, F.; Waller, S.; Malaska, M.; Cable, M. Sampling Accelerated Micron Scale Ice Particles with a Quadrupole Ion Trap Mass Spectrometer. *J. Am. Soc. Mass Spectrom.* **2021**, *32* (5), 1162−1168.

(4) Miller, M. E. C.; Burke, S. E.; Continetti, R. E. Production and Impact Characterization of Enceladus Ice Grain Analogues. *ACS Earth Space Chem.* **2022**, *6*, 1813−1822.

(5) Hudait, A.; Allen, M. T.; Molinero, V. Sink or Swim: Ions and Organics at the Ice-Air Interface. *J. Am. Chem. Soc.* **2017**, *139* (29), 10095−10103.

(6) Farnik, M.; Fedor, J.; Kocisek, J.; Lengyel, J.; Pluharova, E.; Poterya, V.; Pysanenko, A. Pickup and reactions of molecules on clusters relevant for atmospheric and interstellar processes. *Phys. Chem. Chem. Phys.* **2021**, *23* (5), 3195−3213.

(7) Keesee, R. G. Nucleation and Particle Formation in the Upper-Atmosphere. *J. Geophys. Res.: Atmos.* **1989**, *94* (D12), 14683−14692.

(8) Sterpka, C.; Dwyer, J.; Liu, N.; Hare, B. M.; Scholten, O.; Buitink, S.; ter Veen, S.; Nelles, A. The Spontaneous Nature of Lightning Initiation Revealed. *Geophys. Res. Lett.* **2021**, *48* (23), No. e2021GL095511.

(9) Johnston, J. C.; Molinero, V. Crystallization, Melting, and Structure of Water Nanoparticles at Atmospherically Relevant Temperatures. *J. Am. Chem. Soc.* **2012**, *134* (15), 6650−6659.

(10) Hock, C.; Schmidt, M.; Kuhnen, R.; Bartels, C.; Ma, L.; Haberland, H.; von Issendorff, B. Calorimetric Observation of the Melting of Free Water Nanoparticles at Cryogenic Temperatures. *Phys. Rev. Lett.* **2009**, *103* (7), 073401.

(11) Eiroa, C.; Marshall, J. P.; Mora, A.; Montesinos, B.; Absil, O.; Augereau, J. C.; Bayo, A.; Bryden, G.; Danchi, W.; del Burgo, C.; Ertel, S.; Fridlund, M.; Heras, A. M.; Krivov, A. V.; Launhardt, R.; Liseau, R.; Lohne, T.; Maldonado, J.; Pilbratt, G. L.; Roberge, A.; Rodmann, J.; Sanz-Forcada, J.; Solano, E.; Stapelfeldt, K.; Thebault, P.; Wolf, S.; Ardila, D.; Arevalo, M.; Beichmann, C.; Faramaz, V.; Gonzalez-Garcia, B. M.; Gutierrez, R.; Lebreton, J.; Martinez-Arnaiz, R.; Meeus, G.; Montes, D.; Olofsson, G.; Su, K. Y. L.; White, G. J.; Barrado, D.; Fukagawa, M.; Grun, E.; Kamp, I.; Lorente, R.; Morbidelli, A.; Muller, S.; Mutschke, H.; Nakagawa, T.; Ribas, I.; Walker, H. DUst around NEarby Stars. The survey observational results. *Astron. Astrophys.* **2013**, *555*, A11.

(12) Mocker, A.; Bugiel, S.; Auer, S.; Baust, G.; Colette, A.; Drake, K.; Fiege, K.; Grun, E.; Heckmann, F.; Helfert, S.; Hillier, J.; Kempf, S.; Matt, G.; Mellert, T.; Munsat, T.; Otto, K.; Postberg, F.; Roser, H. P.; Shu, A.; Sternovsky, Z.; Srama, R. A 2 MV Van de Graaff accelerator as a tool for planetary and impact physics research. *Rev. Sci. Instrum.* **2011**, *82* (9), 095111.

(13) Zilch, L. W.; Maze, J. T.; Smith, J. W.; Jarrold, M. F. Freezing, fragmentation, and charge separation in sonic sprayed water droplets. *Int. J. Mass Spectrom.* **2009**, *283* (1−3), 191−199.

(14) Smith, J. W.; Siegel, E. E.; Maze, J. T.; Jarrold, M. F. Image charge detection mass spectrometry: Pushing the envelope with sensitivity and accuracy. *Anal. Chem.* **2011**, *83* (3), 950−956.

(15) Jarrold, M. F. Applications of Charge Detection Mass Spectrometry in Molecular Biology and Biotechnology. *Chem. Rev.* **2022**, *122* (8), 7415−7441.

(16) Todd, A. R.; Alexander, A. W.; Jarrold, M. F. Implementation of a Charge-Sensitive Amplifier without a Feedback Resistor for Charge Detection Mass Spectrometry Reduces Noise and Enables Detection of Individual Ions Carrying a Single Charge. *J. Am. Soc. Mass Spectrom.* **2020**, *31* (1), 146−154.

(17) Gombosi, T. I.; Burch, J. L.; Horanyi, M. Negatively charged nano-grains at 67P/Churyumov-Gerasimenko. *Astron. Astrophys.* **2015**, *583*, A23.

(18) Spahn, F.; Schmidt, J.; Albers, N.; Hörning, M.; Makuch, M.; Seiß, M.; Kempf, S.; Srama, R.; Dikarev, V.; Helfert, S.; Moragas-Klostermeyer, G.; Krivov, A. V.; Sremčević, M.; Tuzzolino, A. J.; Economou, T.; Grün, E. Cassini dust measurement at Enceladus and implications for the origin of the E ring. *Science* **2006**, *311* (5766), 1416−1418.

(19) Quick, L. C.; Barnouin, O. S.; Prockter, L. M.; Patterson, G. W. Constraints on the detection of cryovolcanic plumes on Europa. *Planet. Space Sci.* **2013**, *86*, 1−9.

(20) Jones, G. H.; Arridge, C. S.; Coates, A. J.; Lewis, G. R.; Kanani, S.; Wellbrock, A.; Young, D. T.; Crary, F. J.; Tokar, R. L.; Wilson, R. J.; Hill, T. W.; Johnson, R. E.; Mitchell, D. G.; Schmidt, J.; Kempf, S.; Beckmann, U.; Russell, C. T.; Jia, Y. D.; Dougherty, M. K.; Waite, J. H.; Magee, B. A. Fine Jet Structure of Electrically Charged Grains in Enceladus' Plume. *Geophys. Res. Lett.* **2009**, *36* (16), L16204.

(21) Hillier, J. K.; Schmidt, J.; Hsu, H. W.; Postberg, F. Dust Emission by Active Moons. *Space Sci. Rev.* **2018**, *214* (8), 131.

(22) Kruger, H.; Krivov, A. V.; Hamilton, D. P.; Grun, E. Detection of an impact-generated dust cloud around Ganymede. *Nature* **1999**, *399* (6736), 558−560.

(23) Kruger, H.; Krivov, A. V.; Sremcevic, M.; Grun, E. Impact-generated dust clouds surrounding the Galilean moons. *Icarus* **2003**, *164* (1), 170−187.

(24) Goode, W.; Kempf, S.; Schmidt, J. Detecting the surface composition of geological features on Europa and Ganymede using a surface dust analyzer. *Planet. Space Sci.* **2021**, *208*, 105343.

(25) Lunine, J. I.; Coustenis, A.; Mitri, G.; Tobie, G.; Tosi, F. Future Exploration of Enceladus and Other Saturnian Moons. In *Enceladus and the Icy Moons of Saturn*; Schenk, P. M., Clark, R. N., Howett, C. J. A., Verbiscer, A. J., Waite, J. H., Eds.; The University of Arizona Press: 2018; pp 453−468.

(26) Srama, R.; Ahrens, T. J.; Altobelli, N.; Auer, S.; Bradley, J. G.; Burton, M.; Dikarev, V. V.; Economou, T.; Fechtig, H.; Gorlich, M.; Grande, M.; Graps, A.; Grun, E.; Havnes, O.; Helfert, S.; Horanyi, M.; Igenbergs, E.; Jessberger, E. K.; Johnson, T. V.; Kempf, S.; Krivov, A. V.; Kruger, H.; Mocker-Ahlreep, A.; Moragas-Klostermeyer, G.; Lamy, P.; Landgraf, M.; Linkert, D.; Linkert, G.; Lura, F.; McDonnell, J. A. M.; Mohlmann, D.; Morfill, G. E.; Muller, M.; Roy, M.; Schafer, G.; Schlotzhauer, G.; Schwehm, G. H.; Spahn, F.; Stubig, M.; Svestka, J.; Tschernjawski, V.; Tuzzolino, A. J.; Wasch, R.; Zook, H. A. The Cassini Cosmic Dust Analyzer. *Space Sci. Rev.* **2004**, *114* (1−4), 465−518.

(27) Postberg, F.; Kempf, S.; Schmidt, J.; Brilliantov, N.; Beinsen, A.; Abel, B.; Buck, U.; Srama, R. Sodium Salts in E-Ring Ice Grains from an Ocean below the Surface of Enceladus. *Nature* **2009**, *459*, 1098−1101.

(28) Postberg, F.; Schmidt, J.; Hillier, J.; Kempf, S.; Srama, R. A Salt-Water Reservoir as the Source of a Compositionally Stratified Plume on Enceladus. *Nature* **2011**, *474*, 620−622.

(29) Postberg, F.; Khawaja, N.; Abel, B.; Choblet, G.; Glein, C. R.; Gudipati, M. S.; Henderson, B. L.; Hsu, H. W.; Kempf, S.; Klenner, F.; Moragas-Klostermeyer, G.; Magee, B.; Nölle, L.; Perry, M.; Reviol, R.; Schmidt, J.; Srama, R.; Stolz, F.; Tobie, G.; Trieloff, M.; Waite, J. H. Macromolecular organic compounds from the depths of Enceladus. *Nature* **2018**, *558*, 564−568.

(30) Klenner, F.; Postberg, F.; Hillier, J.; Khawaja, N.; Reviol, R.; Srama, R.; Abel, B.; Stolz, F.; Kempf, S. Analogue spectra for impact ionization mass spectra of water ice grains obtained at different impact speeds in space. *Rapid Commun. Mass Spectrom.* **2019**, *33* (22), 1751−1760.

(31) Klenner, F.; Postberg, F.; Hillier, J.; Khawaja, N.; Cable, M. L.; Abel, B.; Kempf, S.; Glein, C. R.; Lunine, J. I.; Hodyss, R.; Reviol, R.; Stolz, F. Discriminating Abiotic and Biotic Fingerprints of Amino Acids and Fatty Acids in Ice Grains Relevant to Ocean Worlds. *Astrobiology* **2020**, *20* (10), 1168−1184.

(32) Klenner, F.; Postberg, F.; Hillier, J.; Khawaja, N.; Reviol, R.; Stolz, F.; Cable, M. L.; Abel, B.; Noelle, L. Analog Experiments for the Identification of Trace Biosignatures in Ice Grains from Extraterrestrial Ocean Worlds. *Astrobiology* **2020**, *20* (2), 179−189.

(33) Szalay, J. R.; Bonfond, B.; Allegrini, F.; Bagenal, F.; Bolton, S.; Clark, G.; Connerney, J. E. P.; Ebert, R. W.; Ergun, R. E.; Gladstone, G. R.; Grodent, D.; Hospodarsky, G. B.; Hue, V.; Kurth, W. S.; Kotsiaros, S.; Levin, S. M.; Louarn, P.; Mauk, B.; McComas, D. J.; Saur, J.; Valek, P. W.; Wilson, R. J. In Situ Observations Connected to the Io Footprint Tail Aurora. *J. Geophys. Res.: Planets* **2018**, *123* (11), 3061−3077.

(34) Kempf, S.; Altobelli, N.; Briois, C.; Grün, E.; Horanyi, M.; Postberg, F.; Schmidt, J.; Srama, R.; Sternovsky, Z.; Tobie, G.; Zolotov, M. In *SUDA: A Dust Mass Spectrometer for Compositional Surface Mapping for a Mission to Europa*; European Planetary Science Congress 2014: 2014; pp EPSC2014−229.

(35) Postberg, F.; Grun, E.; Horanyi, M.; Kempf, S.; Kruger, H.; Schmidt, J.; Spahn, F.; Srama, R.; Sternovsky, Z.; Trieloff, M. Compositional mapping of planetary moons by mass spectrometry of dust ejecta. *Planet. Space Sci.* **2011**, *59* (14), 1815−1825.

(36) Zilch, L. W.; Maze, J. T.; Smith, J. W.; Ewing, G. E.; Jarrold, M. F. Charge Separation in the Aerodynamic Breakup of Micrometer-Sized Water Droplets. *J. Phys. Chem. A* **2008**, *112* (51), 13352−13363.

(37) Maze, J. T.; Jones, T. C.; Jarrold, M. F. Negative droplets from positive electrospray. *J. Phys. Chem. A* **2006**, *110* (46), 12607−12612.

(38) Gao, J. Z.; Austin, D. E. Mechanistic Investigation of Charge Separation in Electrospray Ionization using Microparticles to Record Droplet Charge State. *J. Am. Soc. Mass Spectrom.* **2020**, *31* (10), 2044−2052.

(39) Lee, S. W.; Freivogel, P.; Schindler, T.; Beauchamp, J. L. Freeze-dried biomolecules: FT-ICR studies of the specific solvation of functional groups and clathrate formation observed by the slow evaporation of water from hydrated peptides and model compounds in the gas phase. *J. Am. Chem. Soc.* **1998**, *120* (45), 11758−11765.

(40) Huang, J. F.; Bartell, L. S. Kinetics of Homogeneous Nucleation in the Freezing of Large Water Clusters. *J. Phys. Chem.* **1995**, *99* (12), 3924−3931.

(41) Mizuse, K.; Mikami, N.; Fujii, A. Infrared Spectra and Hydrogen-Bonded Network Structures of Large Protonated Water Clusters H$+(H2O)(n)$ (n = 20−200). *Angew. Chem.-Int. Ed.* **2010**, *49* (52), 10119−10122.

(42) Hansmann, B.; Abel, B. Kinetics in cold laval nozzle expansions: From atmospheric chemistry to oxidation of biomolecules in the gas phase. *ChemPhysChem* **2007**, *8* (3), 343−356.

(43) Buck, U.; Pradzynski, C. C.; Zeuch, T.; Dieterich, J. M.; Hartke, B. A size resolved investigation of large water clusters. *Phys. Chem. Chem. Phys.* **2014**, *16* (15), 6859−6871.

(44) Pradzynski, C. C.; Forck, R. M.; Zeuch, T.; Slavicek, P.; Buck, U. A Fully Size-Resolved Perspective on the Crystallization of Water Clusters. *Science* **2012**, *337* (6101), 1529−1532.

(45) Koizumi, H.; Wang, X. L.; Whitten, W. B.; Reilly, P. T. A. Controlling the Expansion into Vacuum-the Enabling Technology for Trapping Atmosphere-Sampled Particulate Ions. *J. Am. Soc. Mass Spectrom.* **2010**, *21* (2), 242−248.

(46) Wang, X. Y.; Chen, H. J.; Lee, J.; Reilly, P. T. A. Increasing the trapping mass range to m/z = 10(9)-A major step toward high resolution mass analysis of intact RNA, DNA and viruses. *Int. J. Mass Spectrom.* **2012**, *328*, 28−35.

(47) Wilcox, B. E.; Hendrickson, C. L.; Marshall, A. G. Improved ion extraction from a linear octopole ion trap: SIMION analysis and experimental demonstration. *J. Am. Soc. Mass Spectrom.* **2002**, *13* (11), 1304−1312.

(48) Fuerstenau, S. D.; Benner, W. H. Molecular weight determination of megadalton DNA electrospray ions using charge

detection time-of-flight mass spectrometry. *Rapid Commun. Mass Spectrom.* **1995**, *9* (15), 1528−1538.

(49) Keifer, D. Z.; Pierson, E. E.; Jarrold, M. F. Charge detection mass spectrometry: weighing heavier things. *Analyst* **2017**, *142* (10), 1654−1671.

(50) Landais, B.; Beaugrand, C.; Capron-Dukan, L.; Sablier, M.; Simonneau, G.; Rolando, C. Varying the radio frequency: a new scanning mode for quadrupole analyzers. *Rapid Commun. Mass Spectrom.* **1998**, *12* (6), 302−306.

(51) Marmet, P.; Proulx, M. A Frequency-Swept Quadrupole Mass Filter. *Int. J. Mass Spectrom.* **1982**, *42* (1−2), 3−10.

(52) Douglas, D. J. Linear Quadrupoles in Mass Spectrometry. *Mass Spectrom Rev.* **2009**, *28* (6), 937−960.

(53) Gerlich, D. Inhomogeneous Rf-Fields - a Versatile Tool for the Study of Processes with Slow Ions. *Adv. Chem. Phys.* **1992**, *82*, 1−176.

(54) Chernushevich, I. V.; Thomson, B. A. Collisional cooling of large ions in electrospray mass spectrometry. *Anal. Chem.* **2004**, *76* (6), 1754−1760.

(55) Moberg, D. R.; Becker, D.; Dierking, C. W.; Zurheide, F.; Bandow, B.; Buck, U.; Hudait, A.; Molinero, V.; Paesani, F.; Zeuch, T. The end of ice I. *P. Natl. Acad. Sci. USA* **2019**, *116* (49), 24413−24419.

(56) Spanel, P.; Dryahina, K.; Smith, D. A general method for the calculation of absolute trace gas concentrations in air and breath from selected ion flow tube mass spectrometry data. *Int. J. Mass Spectrom.* **2006**, *249*, 230−239.

(57) Koizumi, H.; Whitten, W. B.; Reilly, P. T. Trapping of intact, singly-charged, bovine serum albumin ions injected from the atmosphere with a 10-cm diameter, frequency-adjusted linear quadrupole ion trap. *J. Am. Soc. Mass Spectrom.* **2008**, *19* (12), 1942−7.

(58) Wyttenbach, T.; Bleiholder, C.; Bowers, M. T. Factors Contributing to the Collision Cross Section of Polyatomic Ions in the Kilodalton to Gigadalton Range: Application to Ion Mobility Measurements. *Anal. Chem.* **2013**, *85* (4), 2191−2199.

(59) Davis, E. J.; Bridges, M. A. The Rayleigh Limit of Charge Revisited - Light-Scattering from Exploding Droplets. *J. Aerosol Sci.* **1994**, *25* (6), 1179−1199.

(60) Rayleigh, L.; Lord, X. X. On the Equilibrium of Liquid Conducting Masses Charged with Electricity. *Philos. Mag. Ser.* **1882**, *14*, 184.

(61) Korolev, A.; Leisner, T. Review of experimental studies of secondary ice production. *Atmos. Chem. Phys.* **2020**, *20* (20), 11767−11797.

(62) Qu, X.; Davis, E. J. Droplet evaporation and condensation in the near-continuum regime. *J. Aerosol Sci.* **2001**, *32* (7), 861−875.

(63) Qu, X.; Davis, E. J.; Swanson, B. D. Non-isothermal droplet evaporation and condensation in the near-continuum regime. *J. Aerosol Sci.* **2001**, *32* (11), 1315−1339.

(64) Wilson, K. R.; Rude, B. S.; Smith, J.; Cappa, C.; Co, D. T.; Schaller, R. D.; Larsson, M.; Catalano, T.; Saykally, R. J. Investigation of volatile liquid surfaces by synchrotron x-ray spectroscopy of liquid microjets. *Rev. Sci. Instrum.* **2004**, *75* (3), 725−736.

(65) Smith, J. D.; Cappa, C. D.; Drisdell, W. S.; Cohen, R. C.; Saykally, R. J. Raman thermometry measurements of free evaporation from liquid water droplets. *J. Am. Chem. Soc.* **2006**, *128* (39), 12892−12898.

(66) Espinosa, J. R.; Navarro, C.; Sanz, E.; Valeriani, C.; Vega, C. On the time required to freeze water. *J. Chem. Phys.* **2016**, *145* (21), 211922.

(67) Espinosa, J. R.; Vega, C.; Sanz, E. Ice-Water Interfacial Free Energy for the TIP4P, TIP4P/2005, TIP4P/Ice, and mW Models As Obtained from the Mold Integration Technique. *J. Phys. Chem. C* **2016**, *120* (15), 8068−8075.

(68) Murphy, D. M.; Koop, T. Review of the vapour pressures of ice and supercooled water for atmospheric applications. *Q J. Roy Meteor Soc.* **2005**, *131* (608), 1539−1565.

(69) Xu, Y. T.; Petrik, N. G.; Smith, R. S.; Kay, B. D.; Kimmel, G. A. Growth rate of crystalline ice and the diffusivity of supercooled water from 126 to 262 K. *P. Natl. Acad. Sci. USA* **2016**, *113* (52), 14921−14925.

(70) Archer, D. G.; Carter, R. W. Thermodynamic properties of the NaCl+H2O system. 4. Heat capacities of H2O and NaCl(aq) in cold-stable and supercooled states. *J. Phys. Chem. B* **2000**, *104* (35), 8563−8584.

(71) Pruppacher, H. R. Interpretation of Experimentally Determined Growth Rates of Ice Crystals in Supercooled Water. *J. Chem. Phys.* **1967**, *47* (5), 1807−1813.

(72) Mabbett, S. R.; Zilch, L. W.; Maze, J. T.; Smith, J. W.; Jarrold, M. F. Pulsed acceleration charge detection mass spectrometry: Application-to weighing electrosprayed droplets. *Anal. Chem.* **2007**, *79* (22), 8431−8439.

(73) *CRC Handbook of Chemistry and Physics*; Weast, R. C., Ed.; CRC Press: 1989.

(74) Tang, K.; Gomez, A. Generation by Electrospray of Monodisperse Water Droplets for Targeted Drug-Delivery by Inhalation. *J. Aerosol Sci.* **1994**, *25* (6), 1237−1249.

(75) Tang, K.; Gomez, A. On the Structure of an Electrostatic Spray of Monodisperse Droplets. *Phys. Fluids* **1994**, *6* (7), 2317−2332.

(76) Higuera, F. J. Neutralization of a spray of electrically charged droplets by a corona discharge. *J. Fluid Mech.* **2016**, *801*, 130−149.

(77) Carrasco-Munoz, A.; Barbero-Colmenar, E.; Bodnár, E.; Grifoll, J.; Rosell-Llompart, J. Monodisperse droplets and particles by efficient neutralization of electrosprays. *J. Aerosol Sci.* **2022**, *160*, 105909.

(78) Liu, B. Y. H.; Pui, D. Y. H. Electrical neutralization of aerosols. *J. Aerosol Sci.* **1974**, *5* (5), 465−472.